J Mater Sci (2022) 57:7191–7207

Chemical routes to materials

Unravelling the role of lithium and nickel doping on the defect structure and phase transition of anatase TiO_2 nanoparticles

Antonio Vázquez-López[1,*], David Maestre[1], Ruth Martínez-Casado[1], Julio Ramírez-Castellanos[2], Igor Píš[3,4], Silvia Nappini[4], and Ana Cremades[1]

[1] Department of Materials Physics, Faculty of Physics, Complutense University of Madrid, 28040 Madrid, Spain
[2] Department of Inorganic Chemistry, Faculty of Chemistry, Complutense University of Madrid, 28040 Madrid, Spain
[3] Elettra-Sincrotrone Trieste S.C.P.A., S.S, 14 km 163.5, 34149 Basovizza, Trieste, Italy
[4] IOM-CNR, Laboratorio TASC, S.S. 14 km 163.5, 34149 Basovizza, Trieste, Italy

Received: 4 December 2021
Accepted: 21 March 2022
Published online: 4 April 2022

ABSTRACT

Anatase TiO_2 nanoparticles doped either with Li or Ni have been synthesized via hydrolysis in variable concentrations. Microstructural analysis confirms the high crystallinity of the doped nanoparticles with sizes around 7 nm, while compositional analysis shows low doping below 2% at. Despite the low concentration of dopants, variations in the Raman and Photoluminescence signals were observed in the doped nanoparticles, mainly due to non-stoichiometry and oxygen deficiency promoted by Li or Ni doping. Doping effects associated with Li and Ni were observed by photoelectron spectroscopy and first principle calculations, which associate the appearance of states in the valence band region to oxygen deficiency and Li or Ni doping and lower n-type character induced by Ni doping. Finally, changes in the thermally induced anatase-to-rutile transition (ART) have been also observed in the doped samples, leading to a dopant-promoted faster ART which occurs at lower temperature boosted due to the dopant effect.

Handling Editor: Christopher Blanford.

Address correspondence to E-mail: antvaz01@ucm.es

https://doi.org/10.1007/s10853-022-07122-x

GRAPHICAL ABSTRACT

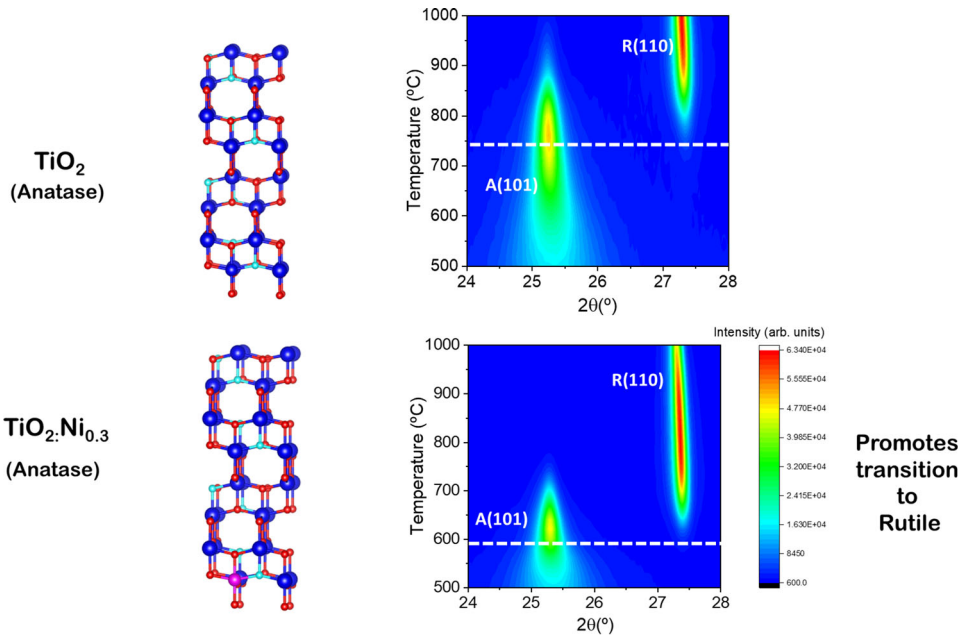

Introduction

During the last decades TiO_2 (titanium dioxide, titania) has become one of the most extensively used wide-band gap semiconductors, mainly in fields of research which can face the modern environmental and energy challenges, such as photocatalysis, solar cells, gas sensors and water splitting. Titania is a low-toxic, inexpensive, biocompatible and chemically stable material which possesses different polymorphs: brookite, anatase and rutile. Both anatase and rutile phases consist of tetragonal structure ($I4_1/amd$ and $P4_2/mnm$, respectively) but differ on their physical and chemical properties such as the refractive index, band gap or electrical conductivity which will determine their applicability. Anatase TiO_2 is commonly used in photocatalysis, solar cells, and lithium-ion batteries (LiBs) [1–3] as it exhibits excellent optoelectronic properties. In particular, anatase possesses higher specific capacity and higher thermodynamic stability than rutile [4], as observed for particles smaller than 20 nm, which has raised interest for this material as a candidate for rechargeable batteries [5], together with its remarkable use as photocatalysis material due to the better photocatalytic activity than rutile TiO_2 [6]. However, anatase can transform into rutile under certain operation conditions, which should be considered in the design of anatase-based devices. In most applications, enhanced properties of TiO_2 are determined not only by the crystallographic phase, but also by the dimensions, structure of defects and doping. Recently, attention has been focused on the investigation based on using metals as dopants, such as Cr, Fe, Al [7–9], or non-metals such as N, C, F, B [3] among many others [10]. Some aspects related to the doping process are not yet understood and deeper insights are required in the study of the effects caused by specific dopants and their variable concentration in the TiO_2 lattice. In this work, a transition metal (Ni) and a monovalent light element (Li) were selected as dopants in anatase TiO_2 nanoparticles in order to analyze the role played by the presence of these elements in the defect structure and physical–chemical properties of anatase TiO_2, with special attention paid

to the effect of the doping in the thermally induced anatase to rutile transition (ART), where they have been labeled as transition promoters [10]. Nickel doping has shown remarkable results in various applications such as photocatalysis [11–13], as a diluted semiconductor (DMS) [14] or in dye-sensitized solar cells [15], while lithium doping has also demonstrated promising results for TiO_2 in catalysis [16], photocatalysis[17], transport layer in perovskite solar cells[18] and or Li-ion batteries [19, 20] being Li-doped TiO_2 regarded as a potential candidate for stable, high-capacity and low toxic anodes with almost twice the specific capacity than undoped TiO_2 [20]. Still, the role between the species valence states and their related defects and the battery performance is not often discussed on metal oxide-based batteries [21]. Understanding the defect structure of doped-titania nanoparticles could contribute to comprehend the improved battery performance, alongside with their improved optoelectronic or photocatalytic properties. In particular, doping in the low concentration regime, below 2% at. is often sufficient to observe major changes on the nanoparticles properties, and therefore this low-doping approach has been considered in this work. When low doping levels and/or light variations in the dopant concentration are required, the control and analysis of the doping could be a difficult task as some of the effects caused by doping can be hardly noticeable or even covered up by some other effects. Hence, highly sensitive techniques and careful analysis of the doped samples, combined with theoretical simulations, are required to assess and exploit the effects caused by low doping.

Among the most common methods to synthesize TiO_2 nanostructures [22], hydrolysis comprises significant advantages, as it is a low-cost and well-controlled method for both undoped and doped nanoparticles which fulfills both the achievement of the desired crystallographic phase and the dopant inclusion, leading to a large and homogeneous quantity of nanomaterial. Furthermore, doping anatase with different elements can control the ART either promoting or hindering the formation of rutile nanoparticles at low temperatures [10], which should be considered in the development of TiO_2 based devices. A deeper characterization of doped titania is needed to understand the mechanism that finally leads to the promotion of this transition.

Herein, we report the study of the morphological, chemical, electronic, luminescent and vibrational properties of undoped and Li or Ni doped anatase TiO_2 nanoparticles synthesized via the hydrolysis method. Low concentrations of each dopant and minor variations in the doping concentrations were selected in order to assess the effects caused by the presence of each dopant in the properties of the anatase TiO_2 nanostructures. In this case, the attention has been focused on the effects induced by slight variations in the Li or Ni doping into the properties of the obtained nanoparticles, for which diverse characterization techniques as well as theoretical simulation were used. Moreover, the thermally induced transition from anatase to rutile was also analyzed as a function of the doping.

The nanoparticles were characterized by X-ray diffraction (XRD), scanning electron microscopy (SEM), X-ray energy dispersive spectroscopy (EDS), inductively coupled plasma optical emission spectrometry (ICP-OES), transmission electron microscopy (TEM) with selected area electron diffraction (SAED), photoluminescence (PL), Raman spectroscopy, synchrotron radiation X-ray photoelectron spectroscopy (XPS) both in and out of resonance, and X-ray absorption spectroscopy (XAS). In addition, first principles calculations have been also performed, obtaining good agreement with the experimental measurements.

Experimental section

Undoped and Li or Ni doped TiO_2 anatase nanoparticles were synthesized by a soft chemical precipitation method based on hydrolysis, which allows to obtain a large quantity of material with good control of size and composition. Titanium (IV) butoxide ($Ti(OBu)_4$, Sigma Aldrich, 97%, liquid content) and 1-butanol (Sigma Aldrich, 99.9% purity, liquid content) were used as precursors, while $NiCl_2{\cdot}6H_2O$ (Probus, solid content) or LiCl (Labkem, 99%, solid content) were also employed for the synthesis of the Ni or Li doped nanoparticles, respectively.

Firstly, undoped TiO_2 nanoparticles were synthesized as a reference. The desired amount by weight of $Ti(OBu)_4$ was selected and 1-butanol, 20 ml per 10 ml of precursor, was added. The mixture was then left with continuous stirring at room temperature and

water was added to induce hydrolysis. The product was centrifuged with distilled water until neutral pH was reached and it was allowed to dry in an oven at 50 °C for at least 12 h, obtaining a fine powder. Finally, a thermal treatment was performed at 250 °C during 24 h to obtain the anatase phase with high crystallinity.

TiO_2 nanoparticles doped with Ni or Li were also synthesized following a similar route. As aforementioned, $Ti(OBu)_4$ and 1-butanol were poured into a flask. Then, the desired stoichiometric amount of the dopant precursors $NiCl_2{\cdot}6H_2O$ or LiCl, respectively, were diluted in the minimum quantity needed of distilled water and then added the flask. After a few seconds of magnetic stirring, distilled water was introduced to induce hydrolysis, and the same post-synthesis treatment as used for the undoped nanoparticles was performed.

Hereafter the nomenclature used for the synthesized nanoparticles is $TiO_2{:}Y_x$, where Y denotes the dopant (Li or Ni), and x = 0.2 and x = 0.3 correspond to the initial concentration (20% or 30% by weight) of the dopant precursors relative to the titanium precursor.

The structural characterization of the nanoparticles was carried out by X-ray diffraction (XRD) with a PANanalytical X'Pert Powder equipment, using the copper Kα line λ_{Cu} = 1.5404 Å. Thermo diffractograms were performed in air with a X'Celerator detector in the range of angles 20–40° using a step size of 0.0334°, at controlled temperatures in the temperature range of 500–1000 °C. The temperature was raised in steps of 20 °C during a controlled-3 min ramp and, after reaching the temperature it was maintained for 13 min while also measuring. The microstructural analysis was performed in a transmission electron microscope [(SAED/TEM) JEM 1400 plus JEOL]. The compositional analysis was carried out by energy dispersive X-ray spectroscopy (EDS) with an EDX Bruker AXS 4010 analyzer coupled to a scanning electron microscope (SEM) Leica 440 Stereoscan. Compositional measurements in the case of lithium doping were made by inductively coupled plasma optical emission spectrometry (ICP-OES) with ICP excitation source, Perkin Elmer Optima 3300DV and SPECTRO Arcos. Photoluminescence (PL) has been studied at room temperature using a confocal microscope with an He-Cd UV laser (λ = 325 nm) as excitation source and collected by a charge coupled device (CCD). Raman measurements have been carried out on a Horiba JobinYvon LabRam Hr800 using a red He–Ne laser (λ = 633 nm). A neutral filter was used to attenuate the total laser intensity, when necessary, diminishing the laser intensity from the nominal 5 mW or 13 mW (I_0), respectively, for the UV or red laser to $0.1{\cdot}I_0$. The laser was focused onto the sample surface using a 40 × objective (numerical aperture = 0.5, Thorlabs LMU-40X-NUV), which produced a laser spot diameter around 1 μm for the UV laser and a few microns for the red laser. The scattered light was collected with the same objective and dispersed with a grating of 600 l/mm for both measurements (PL or Raman) and finally acquired with an air-cooled CCD detector Synapse. Synchrotron radiation X-ray photoelectron (XPS) and X-ray absorption (XAS) spectroscopy have been performed at the CNR Beamline for Advanced diCHroism (BACH) [23, 24] at the Elettra synchrotron facility in Trieste, Italy. The photoelectron spectra were acquired using a Scienta R3000 electron energy analyzer. All core-levels and valence band spectra were recorded with a total energy resolution of 180 meV. For those measurements, samples were prepared as pellets. Binding energies of Ti 2*p* and O 1 s were calibrated to Ti(IV) $2p_{3/2}$ peak set at 458.6 eV. Valence band spectra were referenced to the O2*p*-Ti3*d* bonding peak (7.1 eV). Ni 3*p* and Li 1 s were calibrated to Ti 3 s (62.5 eV). [25] The XAS measurements were performed in total electron yield (TEY) mode by measuring the drain current through the sample. The photon energy resolution was set to 0.15 eV at Ni $L_{3,2}$-edge and O *K*-edge, and to 0.1 eV at Ti $L_{3,2}$ edge.

All Density Functional Theory (DFT) calculations have been performed using the CRYSTAL program, in which the crystalline orbitals are expanded as a linear combination of atom-centered Gaussian orbitals, the basis set. The Ti, O, Li and Ni ions are described using all-electron basis sets contracted as *s*(8) sp(6411) *d*(31), *s*(8) sp(411) *d*(1), *s*(511) *p*(1) *d*(41), *s*(8) sp(6411) *d*(41), respectively. Electronic exchange and correlation were approximated by using the Heyd-Scuseria-Ernzerhof hybrid functional (HSE). In order to meet the required chemical composition, the supercell (2 × 2 × 3) has been considered for $TiO_2{:}Li_{0.2}$, while a (2 × 2 × 2) supercell has been used for $TiO_2{:}Li_{0.3}$, $TiO_2{:}Ni_{0.2}$, and $TiO_2{:}Ni_{0.3}$. The internal coordinates have been determined by minimization of the total energy using an iterative procedure based on the total energy gradient calculated with respect to the nuclear coordinates. Convergence was

determined from the root-mean-square (rms) and the absolute value of the largest component of the forces. The thresholds for the maximum and the rms forces (the maximum and the rms atomic displacements) have been set to 0.00045 and 0.00030 (0.00180 and 0.0012) in atomic units. Geometry optimization was halted when all four conditions were satisfied simultaneously.

Results and discussion

Structural, morphological and chemical characterization

Characterization of the synthesized nanoparticles were initially performed by XRD, as shown in Fig. 1, which confirms that all the XRD patterns can be indexed to the anatase structure of TiO_2 (ICSD n°00-071-1166). The Li or Ni doped samples present an additional weak maximum at around 30.8°, not observed for undoped TiO_2, which can be attributed to brookite TiO_2 (ICSD 00-015-0875). This peak disappears by increasing the temperature of synthesis, however in this case low synthesis temperature of 250 °C was kept in order to prevent grain size increasing and assuring nanosize particles. XRD maxima from the precursors or other oxides or ternary compounds were not detected.

The average crystallite sizes (D) were estimated from the XRD patterns, as shown in Table 1, by using the Scherrer formula $D = 0.89\lambda/B\cos(\theta)$, where B is the FWHM (full width at half maximum) of the diffraction maxima, λ is X-ray wavelength, $K = 0.89$ is the Scherrer factor, and θ corresponds to the Bragg angle. The estimated dimensions from the averaged crystalline domains are around 6–7 nm, with a slight increase for the doped nanoparticles with respect to the undoped ones. Still, small changes can also be attributed to the inherent error of the Scherrer formula application. The corresponding lattice parameters were also estimated from the XRD patters and are shown in Table 1. The complete set of studied particles present similar cell parameter a, while the c parameter presents differences of ± 0.1 Å.

Table 1 Size estimation and cell parameters of the undoped and Li, Ni doped TiO_2 nanoparticles and the corresponding lattice parameters obtained from XRD analysis

Sample	D (nm)	a(Å)	c(Å)
TiO_2	5.9 ± 0.2	3.76(9)	9.35(2)
TiO_2:$Li_{0.2}$	6.3 ± 0.2	3.76(8)	9.26(5)
TiO_2:$Li_{0.3}$	6.2 ± 0.2	3.78(1)	9.45(9)
TiO_2:$Ni_{0.2}$	6.5 ± 0.2	3.76(1)	9.39(3)
TiO_2:$Ni_{0.3}$	6.7 ± 0.2	3.76(6)	9.32(5)

Shifts in the XRD peaks are not observed in Fig. 1 for any of the samples. Li^+ and Ti^{4+} possess similar ionic radii (R_{Li+} = 0.59 Å, R_{Ti4+} = 0.60 Å), hence Li^+ could substitute Ti^{4+} in the anatase TiO_2 lattice without substantial changes in the lattice parameters. In the case of the Ni doped nanoparticles, despite the larger Ni^{2+} ionic radius (R_{Ni2+} = 0.69 Å), a peak shift is neither observed in Fig. 1, which could indicate that Ni is incorporated with variable oxidation states, Ni^{2+} and Ni^{3+}, as they possess a higher and lower ionic radius, respectively. Variable concentration of defects due to each dopant and its concentration should be also considered in the XRD analysis.

EDS and ICP-OES were performed to determine the presence of Ni and Li, respectively, in the nanoparticles. As observed in Table 2, only slight changes in the final dopant incorporation into the TiO_2 lattice were measured, despite the variable initial amount of the corresponding dopant precursor.

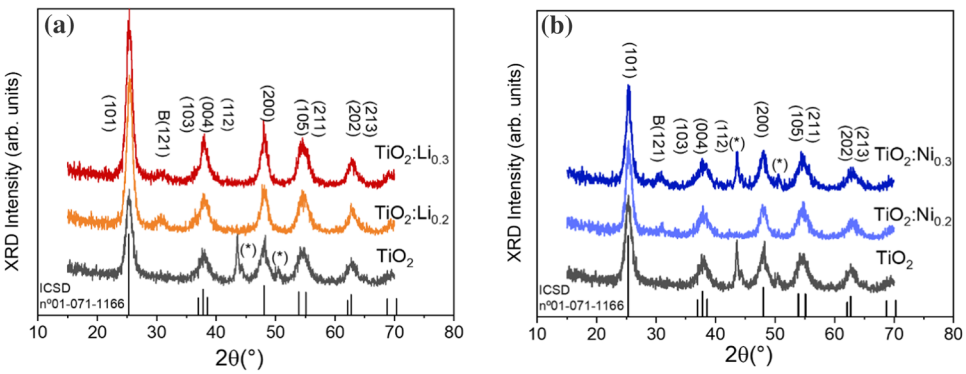

Figure 1 XRD patterns from **a** Lithium and **b** Nickel doped of TiO_2. XRD pattern of undoped TiO_2 is also included as a reference. Peaks labeled with (*) around 43.5–44.5°and 50° are from the sample holder.

Table 2 Compositional analysis of the dopant (Li or Ni) on the doped samples via ICP-OES or EDS, respectively

EDS		ICP-OES	
Sample	Ni content (% at.)	Sample	Li content (% at.)
TiO_2:$Ni_{0.3}$	1.6 ± 0.2	TiO_2:$Li_{0.3}$	0.65 ± 0.02
TiO_2:$Ni_{0.2}$	1.4 ± 0.1	TiO_2:$Li_{0.2}$	0.50 ± 0.03

The amount of Ni varied from 1.4 to 1.6 at.%, while values around 0.5 and 0.65 at.% were measured for Li doping. Hence, nanoparticles with slight differences in the amount of dopants have been synthesized in this work. The remaining element quantification is depicted in Table S1.

Figure 2 displays TEM images of the undoped TiO_2 nanoparticles and the nanoparticles doped with the highest concentration of each dopant. The synthesized nanoparticles show good homogeneity in size, as shown in the TEM images. Averaged particle dimension of 6.9 ± 1.2 nm was estimated for undoped TiO_2, while for TiO_2:$Li_{0.3}$ and TiO_2:$Ni_{0.3}$ averaged dimensions of 7.9 ± 2.1 nm and 8.6 ± 2.5 nm were estimated from the histograms presented as insets. These results are in agreement with XRD measurements which also indicated slightly higher dimensions for the doped nanoparticles. SAED patterns are also presented underneath each TEM image, where a weak diffraction from brookite (1 2 1), as indicated in Fig. 2f, is observed on the TiO_2:$Ni_{0.3}$ sample, in agreement with XRD measurements.

Raman and photoluminescence analysis

Despite the low differences in the dopant concentration, variable doping process and related structure of defects can be promoted in anatase TiO_2 by Li or Ni doping. Raman spectroscopy and Photoluminescence measurements were performed to identify and analyze some of the effects related to the doping process.

Figure 3 shows Raman spectra from the nanoparticles acquired with a He–Ne laser (λ = 633 nm) and using neutral filters in order to avoid a possible anatase to rutile transition induced during laser irradiation. Raman equipment was carefully centered using the silicon 520 cm^{-1} peak in order to distinguish possible peak shifts.

Anatase TiO_2 possesses 15 optical modes with an irreducible representation of 1 A_{1g} + 1 A_{2u} + 2 B_{1g} + 1 B_{2u} + 3 E_g + 2 E_u [26]. Usually Raman

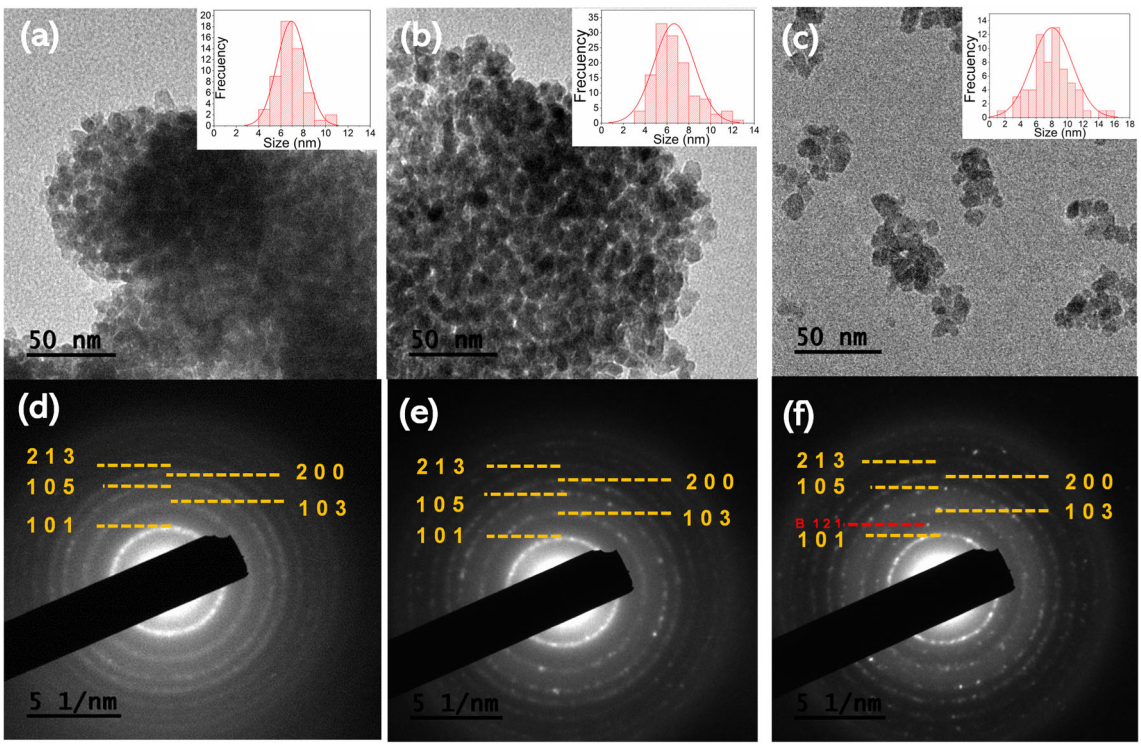

Figure 2 TEM images corresponding to **a** TiO_2 **b** TiO_2:$Li_{0.3}$ and **c** TiO_2:$Ni_{0.3}$ nanoparticles with their corresponding SAED patterns underneath **d, e** and **f**, respectively. Histogram included as insets show the averaged particle sizes for each image.

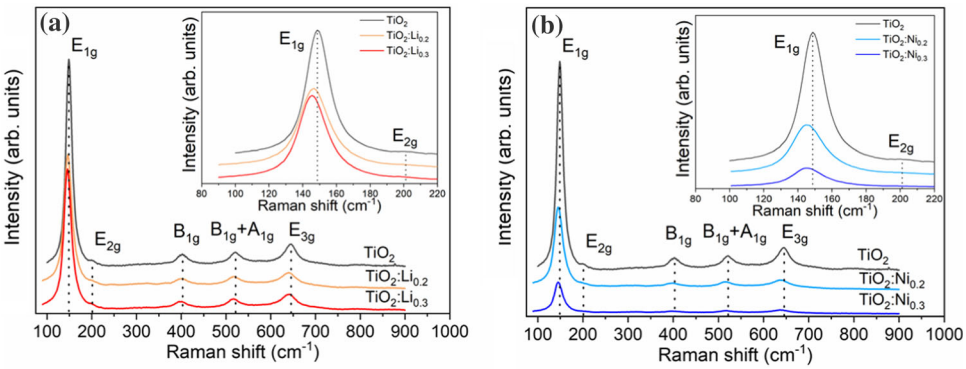

Figure 3 Raman spectra from **a** Li and **b** Ni doped nanoparticles. Raman spectrum from undoped TiO_2 is also included in **a** and **b** as a reference. The E_{1g} mode is enlarged in the insets in **a** and **b** as a function of the type and amount of dopant.

spectroscopy shows six active vibrational modes for anatase TiO_2, which in our case are three E_g modes centered at 149, 199 and 646 cm^{-1}, a B_{1g} mode at 403 and a $A_{1g} + B_{1g}$ mode at 521 cm^{-1},[27]. Some of these modes are especially sensitive to changes in the structural defects and the presence of dopants in the anatase lattice. In particular, the E_g mode is associated with symmetrical stretching vibrations of the O–Ti–O groups, whereas the $A_{1g} + B_{1g}$ (521 cm^{-1}) modes are associated with antisymmetric and symmetric bending vibrations of O−Ti−O groups [9]. For all the samples analyzed in this work, the dominant peak is the E_g mode centered at 149 cm^{-1}. This mode is more sensitive to the concentration of oxygen vacancies in anatase TiO_2 [9, 28]. The total intensity of the Raman signal decreases for the doped samples, especially for the Ni doped ones. Moreover, for the doped samples there is a small redshift in all the modes, mainly for the E_g mode (149 cm^{-1}). This weak redshift is more noticeable for the nickel doped nanoparticles, together with a peak widening, as observed in the insets in Fig. 3. We attribute the observed weak redshift to phonon confinement and non-stoichiometry effects in the doped nanoparticles probably due to the variable presence of oxygen vacancies [27]. Figure S1 shows the variation of the FWHM and the position from the main Raman peaks, obtained by a deconvolution of each Raman mode to Gauss-Lorentz functions after background correction. It can be appreciated that the width of the peaks is higher for the doped samples, despite their slightly higher dimensions. For most of the modes, the FWHM increases for low doping and decreased for a higher amount of dopant. These effects in the Raman signal from the doped nanoparticles can be related to the disruption and contraction of the TiO_2 lattice due to the substitution of Ti^{4+} by Ni^{2+} [29] or Li^+ creating oxygen vacancies. This broadening and peak shift have been also observed in La-[30], Mn-[31] or Mo-[32] doped anatase TiO_2 which assures the effect on the concentration of oxygen vacancies to maintain overall charge neutrality after the dopant inclusion. Peak position of the different Raman modes also changes, while for Mn or Mo doping it has been observed a shift towards higher wavenumber [31, 32] attributed to phonon confinement, Li- or Ni-doping shows a shift towards lower wavenumber which has been attributed to Li ions on TIO_2 nanocrystals[17] as well to size effects in Ni-doped TiO_2[15].

Normalized PL spectra of doped and undoped samples are shown in Fig. 4. All the spectra can be deconvoluted into three main Gaussian contributions at 2.0, 2.36 and 2.85 eV. The emission centered at 2.36 eV, which dominates the PL spectra from all the samples, has been usually attributed to surface defect associated with oxygen deficiency in anatase TiO_2 [9, 31, 33–35]. The high-energy emission around 2.85 eV can be attributed to the presence of self-trapped excitons (STEs) [9, 31, 33–35], usually observed in titanates formed for octahedral TiO_6, while the low-energy emission around 2 eV can be attributed to localized excitons [34]. Li doping does not significantly affect the luminescence of the nanoparticles (Fig. 4a). However, the total intensity of the PL signal slightly decreases for the TiO_2:$Li_{0.2}$ sample, whereas it increases for the nanoparticles with the highest amount of lithium (TiO_2:$Li_{0.3}$), as observed in the supplementary Figure S2. This effect could be related to a disorder induced with Li^+ or the creation of recombination centers of photogenerated electrons and holes [35]. Ni doping promotes the emission centered 2.85 eV (Fig. 4b) attributed to self-trapped excitons, as also reported for Fe-doped anatase TiO_2 [8, 9]. In this case, no significant variations

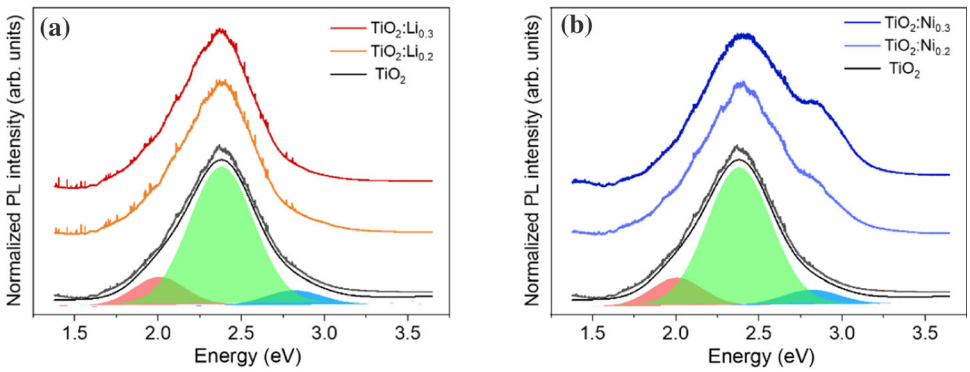

Figure 4 Normalized photoluminescence spectra from **a** Li and **b** Ni doped nanoparticles. Undoped TiO_2 photoluminescence spectrum and its deconvolutions to Gaussian functions are included in both graphs as a reference.

were observed between samples TiO_2:$Ni_{0.2}$ and TiO_2:$Ni_{0.3}$. In both cases Ni-doping induces a decrease in the total intensity of the PL emission, as compared to undoped TiO_2, contrary to the effect observed for Li doping. Some authors reported a decrease in the PL signal for Co- doped TiO_2 related to the formation of non-radiative levels [33], although for Ni doping the localization of Ni trapping levels in the band gap should be also considered [12]. This effect is also supported by DFT calculations which points to a possible reduction of the bandgap and the presence of impurity states for anatase TiO_2 doped with transition metals [36].

According to the Raman and PL analysis, only slight changes are induced by Li or Ni doping in the structure and the luminescence properties of the TiO_2 nanoparticles, in accordance with the minor variations in the concentration of the dopants. Variable structural defects, mainly associated with oxygen deficiency, were observed as a function of the type and amount of dopant. In particular, Ni doping seems to promote more defective nanoparticles. However, as the variation of the dopant concentration in the samples under study is small, these changes are not very noticeable, and their analysis requires more sensitive techniques. Hence, in order to assess possible changes related to the doping process, XPS and XAS measurements were performed to determine changes in the chemical structure of the undoped and doped samples.

XPS and XAS analysis

XPS and XAS measurements can be extremely sensitive to the variations promoted in the anatase TiO_2 nanoparticles even for low differences in the concentration of dopants. Prior to the measurements, the nanoparticles were pressed into pellets. After Shirley background subtraction, XPS peaks were fitted with Voigt functions. Ti 2*p* and O 1 s spectra were normalized to the peak heights. On the other hand, Li 1 s and Ni 3*p* were normalized with respect to Ti 3 s. An initial photon energy of 650 eV was used for the acquisition of the Ti 2*p* core level. Both for undoped and doped samples, the Ti 2*p* spectrum exhibits the usual splitting into Ti $2p_{1/2}$ and Ti $2p_{3/2}$ at energies around 464.4 and 458.6 eV, respectively [37]. The XPS spectra from the undoped and doped samples can be fitted with only one contribution associated with Ti^{4+} in TiO_2, as shown in the inset in Fig. 5a. Other contributions due to the presence of Ti with lower oxidation states were not detected in this case, which indicates high crystallinity for the analyzed nanoparticles. Figure 5b shows the O 1 s core level for the undoped and doped TiO_2 samples (TiO_2:$Ni_{0.3}$ and TiO_2:$Li_{0.3}$). Two main contributions, centered at 529.7 eV (O_I) and 531.3 eV (O_{II}) can be observed in the XPS spectra. The O_I contribution is due to the O^{2-} in the anatase TiO_2 lattice (529.7 eV), while O_{II} (531.3 eV) is a complex contribution commonly associated with the presence of oxygen vacancy related defects [38], hydroxyl groups, or chemisorbed oxygen [39]. Similar spectra are observed for each sample, which confirms that the oxygen environment is similar on the different dopants, even after dopant addition. The Li 1 s core levels from the Li doped TiO_2 samples are shown in Fig. 5c. The XPS spectra are centered at 55.8 eV for TiO_2:$Li_{0.2}$ and 55.9 eV for TiO_2:$Li_{0.3}$ which correspond to Li^+, thereby confirming Li doping in these samples. As expected, the analysis of the Li 1 s signal confirms the lower Li concentration for the sample TiO_2:$Li_{0.2}$, in agreement with the ICP-OES measurements. The area comprised by the Li 1 s peak is comparable to the Ti 3 s peak, and considering their similar cross section, it seems that the Li concentration on the surface is relatively

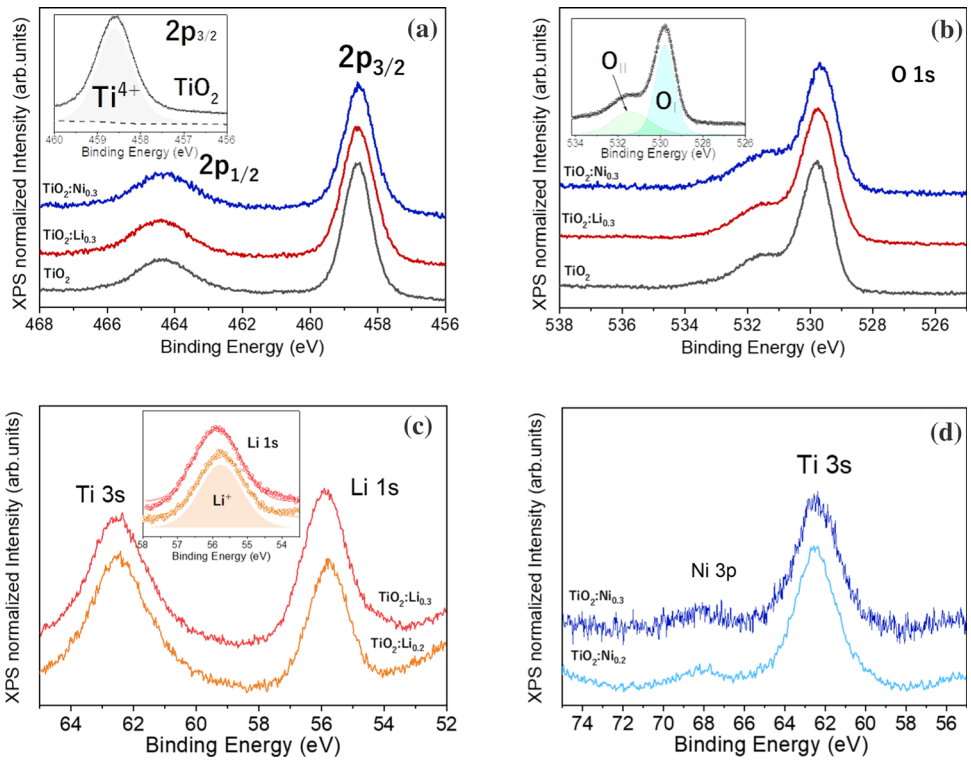

Figure 5 **a** Ti 2*p*, **b** O 1 s, **c** Li 1 s and **d** Ni 3*p* XPS spectra for TiO_2, TiO_2:$Li_{0.3}$ and TiO_2:$Ni_{0.3}$ nanoparticles. A photon energy of 650 eV was used for the acquisition of Ti 2*p*, O 1 s and Ni 3*p* core levels, while a photon energy of 253 eV was employed for the Li 1 s core level. Li 1 s and Ni 3*p* XPS spectra are normalized with respect of Ti 3 s in order to evaluate the differences as a function on the dopant concentration.

high. It has been reported that a large amount of Li^+ was doped onto the surface of TiO_2, probably by the formation of Ti–O–Li bonds [16], and occasionally the lithium migrated to the surface could justify higher nanoparticle size [39], as compared with undoped nanoparticles.

Figure 5d shows Ni 3*p* and Ti 3 s core levels from the Ni doped nanoparticles. The broad contribution in Fig. 5d centered at around 68 eV can be associated with Ni 3*p*, thus reassuring Ni presence in the doped samples. Previous reports show that Ni doping can preserve the Ti^{+4} charge state [38], which agrees with our results.

Figure 6 shows the XAS spectra for TiO_2 nanoparticles doped with the highest dopant concentration, as well as undoped TiO_2 as a reference. Figure 6a shows the Ti $L_{2,3}$-edge associated with the transition of the core electrons from the Ti 2*p* to the unoccupied Ti 3*d* states [40]. Absorption spectra in this work are in good accordance with previous studies on anatase TiO_2 nanostructures [41–43].

Peaks labelled as A and B belong to the L_3 edge while peaks labelled as C and D belongs to the L_2 edge. The splitting of the $L_{2,3}$-edge is due to spin orbit coupling in $L_3(2p_{3/2})$ on the range 454–462 eV, and L_2 $(2p_{1/2})$ on the range 462–467 eV, which are also further split due to crystal field effect into t_{2g} (d_{xy},-d_{xz},d_{yz}) and e_g (d_{z2},d_{x2-y2}) orbitals. The first two peaks in Fig. 6a, labeled as A and A′, are two small pre-peaks related to a transition which is forbidden in LS-coupling, but becomes allowed because of the multi-pole 2*p*-3*d* interactions [42]. The intensity ratio of this doubly-splitted e_g, labeled as B_2, is reversed in anatase and rutile due to the difference of their crystal symmetries [44], being the intensity of B_2 higher than B_2' for anatase, with a ratio $B_2/B_2' > 1$ [45], as observed in this case.

It can be noticed that there are small, but not negligible, variations in the XAS spectra among the probed samples, as observed for the B_2 peaks. It has been reported that either changes or the disappearance of the shoulder B_2 may be due to structure distortions and chemical changes in anatase TiO_2 [46]. In this case, slight variations on the ratio of the relative intensities B_2/B_2' are observed with dopant addition, which for all the samples tends to 1, increasing with the dopant concentration, which might indicate a distortion towards a rutile-like structure. These weak distortions in the XAS spectra observed in the doped nanoparticles could be associated with small changes in the oxygen deficiency, in agreement with Raman and PL measurements.

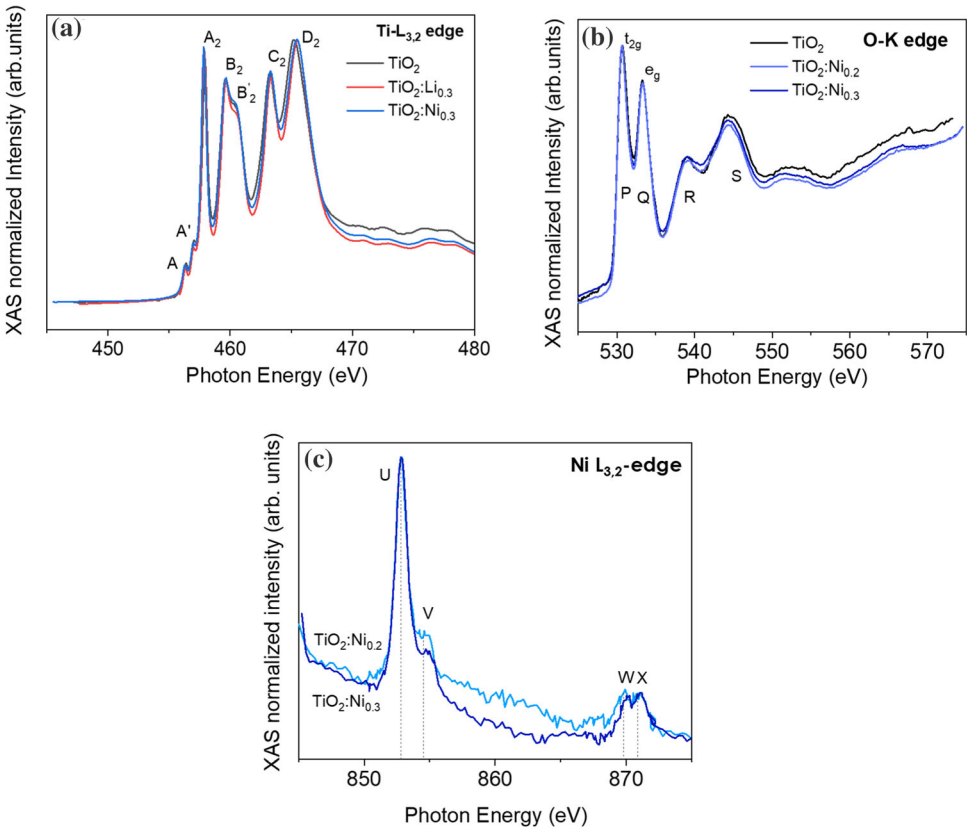

Figure 6 XAS spectra corresponding to **a** Ti $L_{2,3}$-edge, **b** O K-edge, **c** Ni *L*-edge for the TiO_2, TiO_2:$Li_{0.3}$ and TiO_2:$Ni_{0.3}$ nanoparticles.

Figure 6b represents the O-K edge spectra which describes the electronic transition from O 1 s to unoccupied O 2*p* states primarily hybridized with Ti 3*d* unoccupied states. In this case the XAS spectra can be divided in two main regions: (i) 530−536 eV, which reflects the O 2*p*−Ti 3*d* hybridization where, due to crystal field Ti 3*d* splits into t_{2g} π-antibonding states and e_g σ-antibonding states respectively located at 530.6 and 533.3 eV (P and Q peaks), and (ii) > 536 eV (R and S peaks) which reflects the delocalized states derived from the antibonding Ti 4sp/O 2*p* band [45].

The XAS spectrum is sensitive to the electronic environment of the oxygen atoms. Small variations in the relative intensities of the XAS peaks are observed in the XAS spectra for the doped nanoparticles, as compared with undoped TiO_2. Almost no peak broadening is observed which indicates the high crystallinity of the samples even after the dopant inclusion into the crystal lattice. The decrease in the relative intensity of some of these peaks could indicate variations in the oxygen chemical surroundings, as with the titanate octahedral can be distorted due to the dopant inclusion.

Figure 6c represents the Ni $L_{2,3}$ edge of the nickel-doped TiO_2 samples. Similar to Ti *L*-edge, the spectra correspond to the allowed transitions from the Ni 2*p* to the Ni 3*d* states. The splitting in the *L*-edge is due to spin orbit coupling by approximately 17 eV in L_3 ($2p_{3/2}$) in the range 850–855 eV and L_2 ($2p_{1/2}$) in the range of 865–875 eV [47]. Coulomb and exchange interaction between the core holes and the 3*d* shell produces a splitting on the L_3 (U and V) and L_2 (W and X) peaks. The Ni(II) high spin spectra are in agreement with our XAS spectra, as they correspond to the high-energy side of the L_3 peak and a split L_2-edge [47]. This is further in agreement after estimating the ratio $L_3/L_2 + L_3$ with Ni(II), not shown here [48], which indicates that Ni is incorporated in the TiO_2 lattice mainly as Ni^{2+}.

The splitting of L_3 and L_2 into two contributions is very sensitive to the Ni oxidation state and charge transfer. An increase in the relative intensity of these peaks could denote an increase in the hole concentration and thus an increase in the Ni^{3+} concentration [49]. Both TiO_2:$Ni_{0.2}$ and TiO_2:$Ni_{0.3}$ spectra possess comparable relative intensity, thus inducing similar Ni doping in both cases.

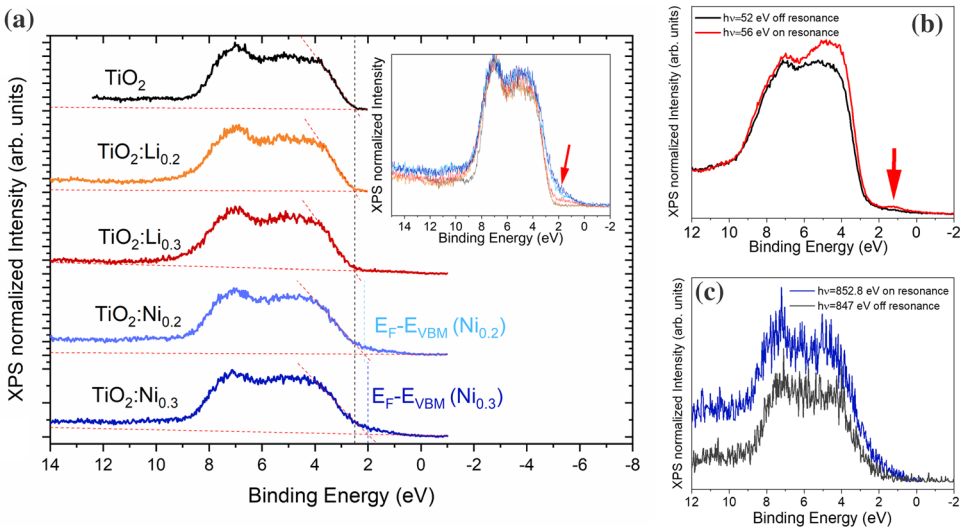

Figure 7 **a** Valence band spectra of undoped and Li or Ni doped TiO_2 nanoparticles acquired with a photon energy of 650 eV. **b** Valence band spectra of the sample TiO_2:$Li_{0.3}$ acquired on-resonance ($h\nu$ = 56 eV) and off-resonance ($h\nu$ = 52 eV). **c** Valence band spectra of the sample TiO_2:$Ni_{0.3}$ acquired on Ni 2*p*-3*d* on-resonance ($h\nu$ = 852.8 eV) and off-resonance ($h\nu$ = 847 eV).

The valence band (VB) region for the undoped and doped TiO_2 nanoparticles are shown in Fig. 7a. The E_F position was calibrated using as reference the O 2*p*-Ti 3*d* bonding peak at ~ 7.1 eV. The energy difference between the Fermi level and the maximum of the valence band (E_F-E_{VBM}) is similar for the undoped and Li doped samples. On the other hand, Ni doped samples show lower E_F-E_{VBM} values than undoped TiO_2 about 0.35 and 0.5 eV for the samples TiO_2:$Ni_{0.2}$ and TiO_2:$Ni_{0.3}$, respectively. Hence, a lower n-type character can be induced by Ni doping. In this case, the presence of acceptor levels induced by Ni doping should be considered. Each VB region is characterized by two broad peaks at ~4.7 and ~7.1 eV mainly related to non-bonding and bonding O 2*p* orbitals, respectively, in accordance with the scientific literature [50]. Differences between the spectra can be observed in the low energy region below 3 eV, as indicated in the inset in Fig. 7a, mainly for the Ni doped samples.

In order to gain deeper insight into the origin of some of these contributions in the VB region, mainly in the low energy region below 3 eV, resonant photoemission spectra were also acquired. This technique is based on changes in the intensity of the photoemission under certain photon energies, as by tuning the incident photon energy across the element specific core-level it is possible to enhance the related states in the valence band or in the band gap. On-resonance photoemission spectra (RPES) for the Ni and Li states were acquired using energies of 852.8 eV, for the sample TiO_2:$Ni_{0.3}$, and 56 eV for TiO_2:$Li_{0.3}$; for the case of Nickel based on the XAS measurements shown in Fig. 6c. For the off-resonance measurements, XPS spectra at photon energies of 847 eV and 52 eV, respectively, were used.

Figure 7b shows RPES spectra for TiO_2:$Li_{0.3}$. There are two clear resonant features around ~4.7 and ~7.1 eV, respectively, related to non-bonding and bonding O 2*p* orbitals, as previously mentioned, and a weak resonant peak at ~ 1.2 eV, marked with an arrow in Fig. 7b. The former and latter contribution observed at ~ 4.7 eV and ~ 7.1 eV, respectively, possess their resonance maximum at 58 eV, as observed in Figure S3. The origin of these peaks can be understood as they were recorded at constant initial state (CIS), hence a plot at CIS of the different intensity vs. photon energy at the positions of 4.7, 7.1 and around 1 eV are plotted. The weak resonant peak at ~ 1 eV becomes also significant on the range of 54–66 eV. CIS spectra show a clear maximum at around 55 eV in agreement with the Li 1 s transition, contrary to the Ti^{3+} related origin reported by other authors. Some authors have indicated the presence of a feature around 0.9 eV, similar to that observed in this work for Li doped TiO_2, which can be associated with a Ti^{3+} 3*d* defect state [50] due to the probability of transition between Ti 3*p*Ti 4 s. Even though previous results on the Ti 2*p* spectra did not show any trace of Ti^{3+}, its presence cannot be completely disregarded in the samples under study. This feature can be attributed also to surface-layer disorders in lithium doped samples [51], similar to other light-element doped anatase samples.

Resonances appear also in the VB region for the TiO_2:$Ni_{0.3}$ sample (Fig. 7c), which exhibit larger

variations as compared to the Li doped samples. We observe not only that the aforementioned peak at ~4.7 eV becomes dominant but also a clear shoulder at ~2.5 eV (marked with an arrow in the inset in Fig. 7a) becomes significant due to Ni-related states which resonate. This feature at 2.5 eV could be related to Ni 3*d* states [52]. A similar feature was reported for Fe-doped TiO_2 [50] attributed as Fe-3*d* and Ti-3*d* derived states. In our case Ni 3*d* could play a role similar to Fe 3*d*.

According to XPS and XAS results as well as previous PL and Raman measurements, the as-synthesized nanoparticles exhibit high crystallinity. Doping process leads to a higher concentration of oxygen vacancies in Li doped TiO_2, while Ni doping induces in addition some other defects, as observed by PL, some of which are probably associated with acceptor levels. Dopant-related states were also promoted in these nanoparticles. In particular Li or Ni-related states were observed in the VB region at ~1 and 2.5 eV, respectively.

First-principles calculations

To assess the effect of both the dopants and the oxygen vacancies on the electronic structure of anatase TiO_2, first principles calculations were performed within the DFT method. Lattice parameters, shown in Table 3, of a = 3.77 Å and c = 9.65 Å have been obtained in agreement with the experimental results presented in Table 1.

The considered concentration of Li and Ni dopants can be seen in Table S2, which have been slightly overestimated with respect to the ones obtained by ICP-OES and EDS to observe more clearly the effect of the dopant concentration on the Density of States (DOS). Several substitutional positions have been studied in order to find the most stable configuration. A 12.5% of oxygen vacancies were introduced in each sample to match the experimental results. The most stable structures and projected DOS are shown in Fig. 8 for TiO_2, TiO_2:$Li_{0.3}$ and TiO_2:$Ni_{0.3}$. Figure 8a shows that undoped TiO_2 under the presence of oxygen vacancies promotes the formation of middle gap states coming from oxygen.

Table 3 Cell parameters of the undoped and Li, Ni doped TiO_2 nanoparticles obtained from DFT calculations

Sample	a(Å)	c(Å)
TiO_2	3.767	9.655
TiO_2:$Li_{0.2}$	3.771	9.644
TiO_2:$Li_{0.3}$	3.768	9.659
TiO_2:$Ni_{0.2}$	3.767	9.655
TiO_2:$Ni_{0.3}$	3.760	9.594

The presence of the V_O defect results in displacements of the Ti and O atoms outward and inward, respectively, from the V_O site [53] which translates to changes in the DOS.

Li does not seem to play a major role on the electronic structure of anatase, as it can be seen in Fig. 8b, where the appearing states are due again to the oxygen atoms. However, Ni doping introduces a variety of states in the bandgap and close to the valence band, as shown in Fig. 8c, reaffirming the results observed by XPS and RPES which show larger variations in the valence band region for the Ni doped samples. Ni doped TiO_2 shows a rather complex role in the VB, in combination with oxygen vacancies, which may play a role on its ferromagnetic effects [14]. Previous studies have shown that the increasing of Ni doping favors rutile structure over anatase [13]. Ni has been reported to decrease the band gap as well as to introduce intra-band gap states. This effect has been observed with our calculations as it can be clearly observed in Fig. 8c. The bandgap values estimated by DFT calculations are shown in Table S2. In all cases the bandgap for anatase was overestimated, however a clear tendency of bandgap narrowing in the doped samples is observed. The discrepancies between the DFT and measured values have been discussed on the literature and are due to the differences on the computational methods [54].

Anatase to rutile transition (ART)

Finally based on the detailed insights achieved in the study of the Li or Ni doped TiO_2, the effects due to the doping process and the related structure of defects in TiO_2 were exploited in the further understanding of the anatase to rutile transition (ART). Anatase transforms irreversibly to the more stable rutile at high temperatures. The range of temperatures at which the ART occurs is affected by the presence of defects and vacancies. Hence, doping engineering is a certain method to control this phase transition, which usually occurs most commonly at around 600 °C for undoped TiO_2 in absence of impurities or dopants [10], but reported transition temperatures vary in a wide range between

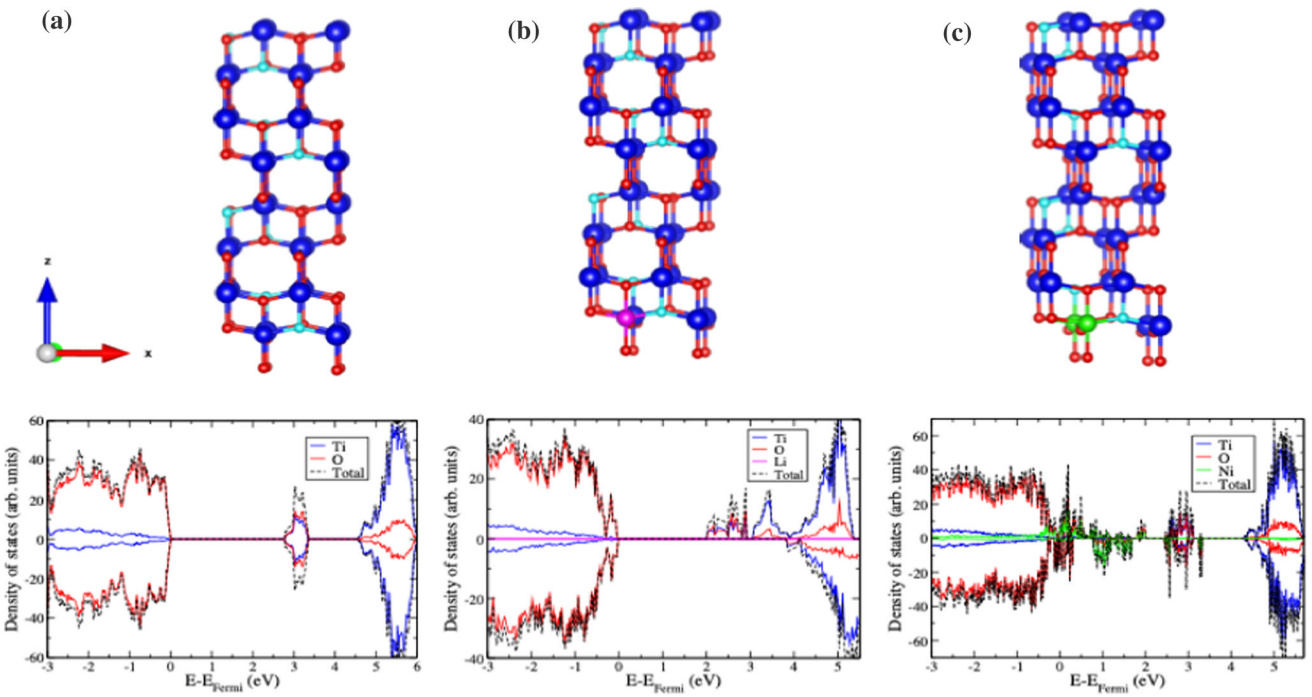

Figure 8 Most stable structures **a** TiO_2, **b** TiO_2:$Li_{0.3}$ and **c** TiO_2:$Ni_{0.3}$ with Ti (blue), O (red), Li (magenta) or Ni (green). Oxygen vacancies are plotted on cyan. Underneath images show the projected DOS for each of the structures shown above.

depending on the use of different synthesis methods materials, dopants, particle size or atmosphere. The ART ranges has been modified by doping, as previously reported by various authors [9, 10, 29, 55, 56], which is an important aspect to be considered in the potential applicability of the anatase phase in devices which operate at high temperatures.

To assess changes in the phase transition promoted in the undoped and doped nanoparticles, thermo-diffraction measurements have been performed in a range of temperatures between 500 and 1000 °C. In this work, the anatase to rutile transition was induced by thermal annealing and probed by thermo-diffraction analysis. Figure 9 depicts the XRD patterns as a function of the temperature in a region between 24 and 28° for TiO_2, TiO_2:$Li_{0.3}$ and TiO_2:$Ni_{0.3}$. A characteristic (101) peak from anatase at 25.3°, and (110) peak from rutile at 27.3° were selected to monitor the ART. These peaks are marked in Fig. 9 as A(101) and R(110), respectively.

As the annealing temperature increases, the diffraction peaks become narrower due to the increase in the dimensions of the nanoparticles, as expected. As observed in Fig. 9a–c the ART begins at around 740 °C for undoped TiO_2, while this transition is initiated at lower temperatures, around 620 and 700 °C, for the Li and Ni doped TiO_2, respectively, being in agreement with the values reported for doped titania by other authors [10, 55, 56] No significant differences have been observed in the ART as a function of the amount of dopants (Fig. 9d), although it should be taken into account that only slight changes on the final concentration of dopants were achieved in this work. Changes on the ART transition as a function of the dopant can be quantified from the analysis of the XRD patterns based on the estimation of the rutile fraction volume following the theory proposed by Spurr and Myers [57] and modified by other authors [32, 58], as shown in Fig S4. Between the different doped nickel nanoparticles the differences in the ART are more notorious than between the different Lithium concentrations. Moreover, the range of temperatures in which the ART occurs is also shorter for the doped samples, especially for the TiO_2:$Ni_{0.3}$ sample, which means a faster kinetics for the ART promoted by doping. Diverse authors reported that the presence of oxygen vacancies facilitates the atoms rearrangement required for the anatase to rutile transition, while the presence of Ti^{3+} interstitials could hinder this transition [9, 10]. In our case, Ni and mainly Li doping could promote the presence of oxygen deficiency in the TiO_2 lattice as Li

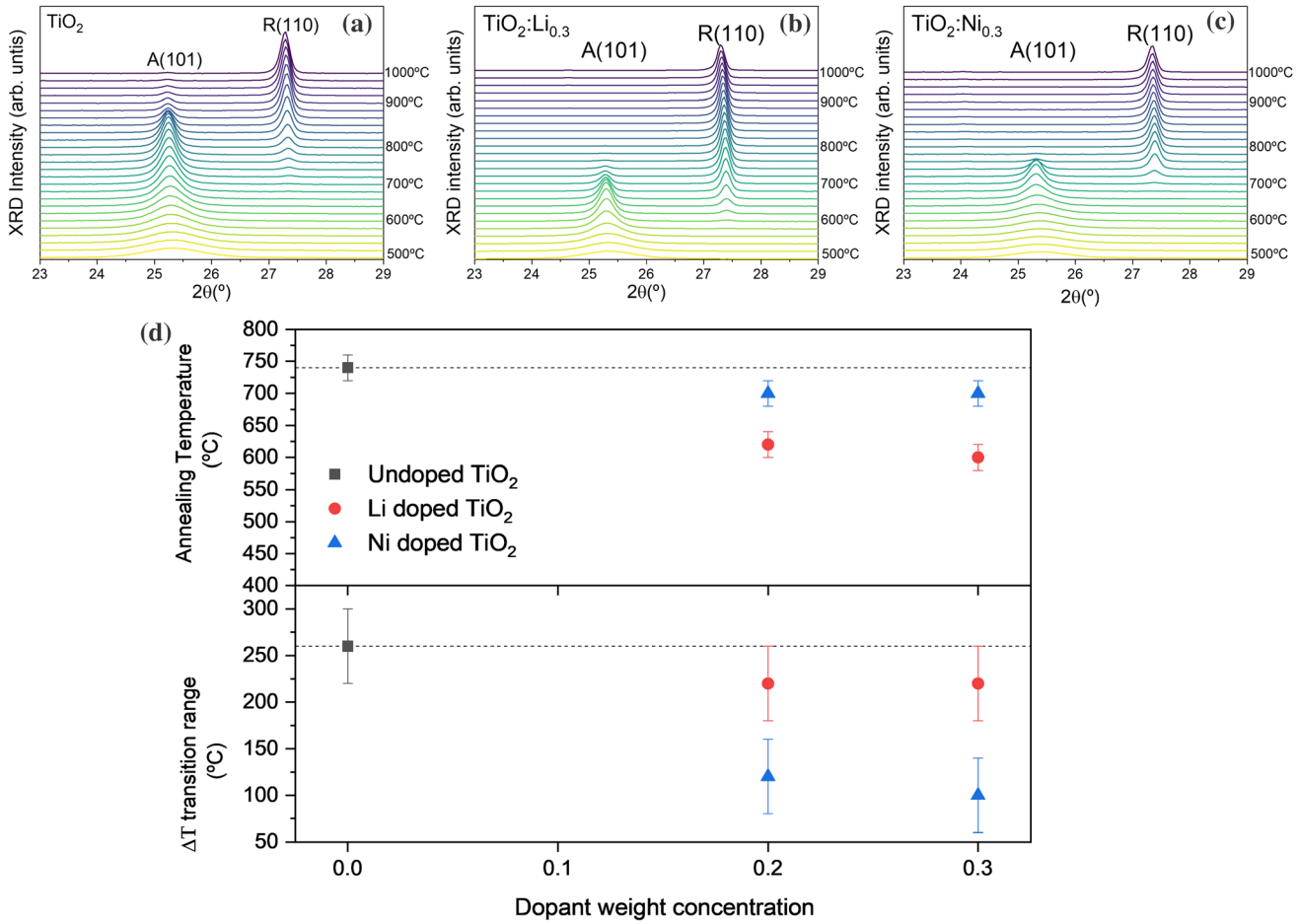

Figure 9 X-ray thermo-diffractograms acquired on the range 500–1000 °C from samples **a** TiO_2, **b** TiO_2:$Li_{0.3}$ and **c** TiO_2:$Ni_{0.3}$. **d** Annealing temperature and range of temperatures for the ART for TiO_2, TiO_2:$Li_{0.3}$ and TiO_2:$Ni_{0.3}$.

and Ni-related defects may contribute to the formation of oxygen vacancies, which are nucleation centers [56]. This is in agreement with Raman and Photoluminescence results which show an increase of oxygen vacancies due to the dopant addition. As mentioned, similar ionic radii of Ni^{2+} and Li^{+} with respect to Ti^{4+} could be translated to the dopants inclusion as interstitials and oxygen vacancies can be created to maintain charge balance. Besides, Ni^{2+} and Li^{+} eases the breaking and creation of Ti–O bonds and modify the kinetics of the ART leading to a promotion of the nucleation and growth process for rutile[10].

Conclusions

Anatase TiO_2 nanoparticles doped with Li or Ni have been synthesized via hydrolysis method. The nanoparticles show high crystallinity and homogeneous dimensions around 7 nm, based on XRD and TEM measurements. Dopant inclusion was confirmed and quantified with EDS and ICP-OES analysis which confirm low doping regime below 2% at. Raman spectroscopy shows slight changes due to the doping process, as red-shift and peak broadening in the doped samples related to non-stoichiometry and changes in the TiO_2 defect structure induced by doping. An increase of the concentration of oxygen vacancies in the doped samples was observed by photoluminescence, mainly in the Li doped ones. Besides, Ni doping promotes an emission at around 2.8 eV associated with self-trapped excitons. As demonstrated by XPS Ti is present as Ti^{4+} both in

undoped and doped nanoparticles, confirming the high crystallinity of the nanoparticles. Ni doping, mainly as Ni^{2+}, also promotes a lower n-type character in the samples. XAS spectra confirm the presence of oxygen deficiencies on the samples with higher dopant concentration. Resonant XPS demonstrates the presence of weak contributions at around 1 eV and 2.5 eV, which can be associated with Li and Ni related states in the valence band. DFT calculations reinforces the effects on the DOS due to both oxygen vacancies and dopants, observing that Ni introduces states near the valence band. Variations in the ART has been also promoted by doping, leading to a decrease in the temperature at which this transition occurs, mainly by Li doping, as confirmed by thermo-XRD measurements. Ni doping promotes as well faster kinetics in the ART. These effects can be related to the structure of defects and oxygen deficiency induced by doping which can ease ART. The achieved deeper knowledge on the Li or Ni doped anatase TiO_2 and the anatase-to-rutile transition could widen the applicability of these nanoparticles in optoelectronic, energy storage and photocatalytic devices.

Acknowledgement

We acknowledge Elettra Sincrotrone Trieste for providing access to its synchrotron radiation facilities. This work was supported by MINECO/FEDER/M-ERA.Net Cofound projects: RTI2018-097195-B-I00 and PCIN-2017-106. I.P. and S.N. gratefully acknowledge financial support from EUROFEL.

Declarations

Conflict of interest The authors declare that they have no conflict of interest.

Supplementary Information: The online version contains supplementary material available at https://doi.org/10.1007/s10853-022-07122-x.

References

[1] Noman MT, Ashraf MA, Ali A (2019) Synthesis and applications of nano-TiO_2: a review. Environ Sci Pollut Res 26:3262–3291. https://doi.org/10.1007/s11356-018-3884-z

[2] Zhang Y, Jiang Z, Huang J et al (2015) Titanate and titania nanostructured materials for environmental and energy applications: a review. RSC Adv 5:79479–79510. https://doi.org/10.1039/c5ra11298b

[3] Schneider J, Matsuoka M, Takeuchi M et al (2014) Understanding TiO_2 photocatalysis: mechanisms and materials. Chem Rev 114:9919–9986. https://doi.org/10.1021/cr5001892

[4] Madian M, Eychmüller A, Giebeler L (2018) Current advances in TiO_2-based nanostructure electrodes for high performance lithium ion batteries. Batteries 4:7. https://doi.org/10.3390/BATTERIES4010007

[5] Liang S, Wang X, Cheng YJ et al (2022) Anatase titanium dioxide as rechargeable ion battery electrode-a chronological review. Energy Storage Mater 45:201–264. https://doi.org/10.1016/J.ENSM.2021.11.023

[6] Zhang J, Zhou P, Liu J, Yu J (2014) New understanding of the difference of photocatalytic activity among anatase, rutile and brookite TiO_2. Phys Chem Chem Phys 16:20382–20386. https://doi.org/10.1039/c4cp02201g

[7] Ahmed SA (2017) Ferromagnetism in Cr-, Fe-, and Ni-doped TiO_2 samples. J Magn Magn Mater 442:152–157. https://doi.org/10.1016/J.JMMM.2017.06.108

[8] Komaraiah D, Radha E, Kalarikkal N et al (2019) Structural, optical and photoluminescence studies of sol-gel synthesized pure and iron doped TiO_2 photocatalysts. Ceram Int 45:25060–25068. https://doi.org/10.1016/J.CERAMINT.2019.03.170

[9] Vásquez GC, Peche-Herrero MA, Maestre D et al (2014) Influence of Fe and Al doping on the stabilization of the anatase phase in TiO_2 nanoparticles. J Mater Chem C 2:10377–10385. https://doi.org/10.1039/c4tc02099e

[10] Hanaor DAH, Sorrell CC (2011) Review of the anatase to rutile phase transformation. J Mater Sci 46:855–874. https://doi.org/10.1007/s10853-010-5113-0

[11] Pirsaheb M, Shahmoradi B, Khosravi T et al (2016) Solar degradation of malachite green using nickel-doped TiO_2 nanocatalysts. Desalin Water Treat 57:9881–9888. https://doi.org/10.1080/19443994.2015.1033764

[12] Hyun Kim D, Sub Lee K, Kim Y-S et al (2006) Photocatalytic activity of Ni 8 wt%-Doped TiO_2 photocatalyst synthesized by mechanical alloying under visible light. J Am Ceram Soc 89:515–518. https://doi.org/10.1111/j.1551-2916.2005.00782.x

[13] Elahifard MR, Ahmadvand S, Mirzanejad A (2018) Effects of Ni-doping on the photo-catalytic activity of TiO_2 anatase and rutile: simulation and experiment. Mater Sci Semicond Process 84:10–16. https://doi.org/10.1016/j.mssp.2018.05.001

[14] Chen J, Lu GH, Cao H et al (2008) Ferromagnetic mechanism in Ni-doped anatase TiO_2. Appl Phys Lett 93:172504. https://doi.org/10.1063/1.3002291

[15] Balakrishnan M, John R (2021) Impact of Ni metal ion concentration in TiO_2 nanoparticles for enhanced photovoltaic performance of dye sensitized solar cell. J Mater Sci Mater Electron 32:5295–5308. https://doi.org/10.1007/S10854-020-05100-0/TABLES/5

[16] Liang Y, Su K, Cao L, Li Z (2019) Lithium doped TiO_2 as catalysts for the transesterification of bisphenol-A with dimethyl carbonate. Mol Catal 465:16–23. https://doi.org/10.1016/j.mcat.2018.12.022

[17] Ravishankar TN, Nagaraju G, Dupont J (2016) Photocatalytic activity of Li-doped TiO_2 nanoparticles: synthesis via ionic liquid-assisted hydrothermal route. Mater Res Bull 78:103–111. https://doi.org/10.1016/j.materresbull.2016.02.017

[18] Lan C, Luo J, Lan H et al (2018) Enhanced charge extraction of Li-doped TiO_2 for efficient thermal-evaporated Sb_2S_3 thin film solar cells. Materials (Basel) 11:355. https://doi.org/10.3390/ma11030355

[19] Wang YQ, Gu L, Guo YG et al (2012) Rutile-TiO_2 nanocoating for a high-rate $Li_4Ti_5O_{12}$ anode of a lithium-ion battery. J Am Chem Soc 134:7874–7879. https://doi.org/10.1021/ja301266w

[20] Vázquez-López A, García-Carrión M, Hall E et al (2021) Hybrid materials and nanoparticles for hybrid silicon solar cells and Li-ion batteries. J Energy Power Technol 3:1–1. https://doi.org/10.21926/JEPT.2102020

[21] Vázquez-López A, Maestre D, Ramírez-Castellanos J et al (2020) Influence of doping and controlled Sn charge state on the properties and performance of SnO_2 nanoparticles as anodes in Li-ion batteries. J Phys Chem C 124:18490–18501. https://doi.org/10.1021/acs.jpcc.0c06318

[22] Nyamukamba P, Okoh O, Mungondori H, et al (2018) Synthetic methods for titanium dioxide nanoparticles: a review. In: Yang D (ed) Titanium dioxide - material for a sustainable environment, IntechOpen. https://doi.org/10.5772/intechopen.70290

[23] Zangrando M, Finazzi M, Paolucci G et al (2001) BACH, the beamline for advanced dichroic and scattering experiments at ELETTRA. Rev Sci Instrum 72:1313–1319. https://doi.org/10.1063/1.1334626

[24] Zangrando M, Zacchigria M, Finazzi M et al (2004) Polarized high-brilliance and high-resolution soft X-ray source at ELETTRA: the performance of beamline BACH. Rev Sci Instrum 75:31–36. https://doi.org/10.1063/1.1634355

[25] Oku M, Wagatsuma K, Kohiki S (1999) Ti 2p and Ti 3p X-ray photoelectron spectra for TiO_2, $SrTiO_3$ and $BaTiO_3$. Phys Chem Chem Phys 1:5327–5331. https://doi.org/10.1039/a907161j

[26] Ohsaka T, Izumi F, Fujiki Y (1978) Raman spectrum of anatase, TiO_2. J Raman Spectrosc 7:321–324. https://doi.org/10.1002/jrs.1250070606

[27] Zhang WF, He YL, Zhang MS et al (2000) Raman scattering study on anatase TiO_2 nanocrystals. J Phys D Appl Phys 33:912–916. https://doi.org/10.1088/0022-3727/33/8/305

[28] Vázquez-López A, Yaseen A, Maestre D et al (2020) Improved silicon surface passivation by hybrid composites formed by PEDOT: PSS with anatase TiO_2 nanoparticles. Mater Lett 271:127802. https://doi.org/10.1016/j.matlet.2020.127802

[29] Xu Z, Wang S, Ma C et al (2019) Effect of nickel doping on phase transformation of TiO_2 nanotube arrays. Phys status solidi 216:1800836. https://doi.org/10.1002/pssa.201800836

[30] Šćepanović M, Aškrabić S, Berec V, Golubović A, Dohčević-Mitrović Z, Kremenović A, Popović ZV (2009) Characterization of La-doped TiO_2 nanopowders by Raman spectroscopy. Acta Phys Pol A 115:771–774

[31] Choudhury B, Choudhury A (2013) Oxygen vacancy and dopant concentration dependent magnetic properties of Mn doped TiO_2 nanoparticle. Curr Appl Phys 13:1025–1031. https://doi.org/10.1016/j.cap.2013.02.007

[32] Kumaravel V, Rhatigan S, Mathew S et al (2020) Mo doped TiO_2: impact on oxygen vacancies, anatase phase stability and photocatalytic activity. J Phys Mater 3:25008. https://doi.org/10.1088/2515-7639/ab749c

[33] Choudhury B, Choudhury A (2012) Luminescence characteristics of cobalt doped TiO_2 nanoparticles. J Lumin 132:178–184. https://doi.org/10.1016/j.jlumin.2011.08.020

[34] Zhang J, Chen X, Shen Y et al (2011) Synthesis, surface morphology, and photoluminescence properties of anatase iron-doped titanium dioxide nano-crystalline films. Phys Chem Chem Phys 13:13096–13105. https://doi.org/10.1039/c0cp02924f

[35] Jiang H, Song H, Zhou Z et al (2007) The roles of Li^+ and F^- ions in Li-F^- codoped TiO_2 system. J Phys Chem Solids 68:1830–1835. https://doi.org/10.1016/j.jpcs.2007.01.027

[36] Zhao YF, Li C, Lu S et al (2016) Effects of oxygen vacancy on 3d transition-metal doped anatase TiO_2: first principles calculations. Chem Phys Lett 647:36–41. https://doi.org/10.1016/j.cplett.2016.01.040

[37] NIST standard reference database (2000) NIST X-ray Photoelectron Spectroscopy Database, NIST Standard Reference Database Number 20, National Institute of Standards and Technology, Gaithersburg MD. https://doi.org/10.18434/T4T88K

[38] Tian J, Gao H, Kong H et al (2013) Influence of transition metal doping on the structural, optical, and magnetic properties of TiO_2 films deposited on Si substrates by a sol-gel process. Nanoscale Res Lett 8:1–11. https://doi.org/10.1186/1556-276X-8-533

[39] Kallel W, Bouattour S, Ferreira LFV, Botelho do Rego AM, (2009) Synthesis, XPS and luminescence (investigations) of Li^{+} and/or Y^{3+} doped nanosized titanium oxide. Mater Chem Phys 114:304–308. https://doi.org/10.1016/j.matchemphys.2008.09.032

[40] Kumar Vishwakarma A, Majid SS, Yadava L (2019) XANES analysis and structural properties of CdS-doped TiO_2. Vacuum 165:239–245. https://doi.org/10.1016/j.vacuum.2019.04.040

[41] Crocombette JP, Jollet F (1994) Ti 2p X-ray absorption in titanium dioxides (TiO_2): the influence of the cation site environment. J Phys Condens Matter 6(49):10811. https://doi.org/10.1088/0953-8984/6/49/022

[42] de Groot FMF, Figueiredo MO, Basto MJ et al (1992) 2 p X-ray absorption of titanium in minerals. Phys Chem Miner 19:140–147. https://doi.org/10.1007/BF00202101

[43] Thomas AG, Flavell WR, Mallick AK et al (2007) Comparison of the electronic structure of anatase and rutile TiO_2 single-crystal surfaces using resonant photoemission and X-ray absorption spectroscopy. Phys Rev B Condens Matter Mater Phys 75:1–12. https://doi.org/10.1103/PhysRevB.75.035105

[44] Kapilashrami M, Zhang Y, Liu YS et al (2014) Probing the optical property and electronic structure of TiO_2 nanomaterials for renewable energy applications. Chem Rev 114:9662–9707. https://doi.org/10.1021/cr5000893

[45] Ruus R, Kikas A, Saar A et al (1997) Ti 2p and O 1s X-ray absorption of TiO_2 polymorphs. Solid State Commun 104:199–203. https://doi.org/10.1016/S0038-1098(97)00300-1

[46] Chen SC, Sung KY, Tzeng WY et al (2013) Microstructure and magnetic properties of oxidized titanium nitride thin films in situ grown by pulsed laser deposition. J Phys D Appl Phys. https://doi.org/10.1088/0022-3727/46/7/075002

[47] Wang H, Ralston CY, Patil DS et al (2000) Nickel L-edge soft X-ray spectroscopy of nickel–iron hydrogenases and model compounds evidence for high-spin nickel(II) in the active enzyme. J Am Chem Soc 122:10544–10552. https://doi.org/10.1021/ja000945g

[48] Gu W, Wang H, Wang K (2014) Nickel L-edge and K-edge X-ray absorption spectroscopy of non-innocent $Ni[S_2C_2(CF_3)_2]_2^n$ series ($n = -2, -1, 0$): direct probe of nickel fractional oxidation state changes. J Chem Soc Dalt Trans 43:6406–6413. https://doi.org/10.1039/c4dt00308j

[49] Lin F, Nordlund D, Weng TC et al (2013) Hole doping in al-containing nickel oxide materials to improve electrochromic performance. ACS Appl Mater Interfaces 5:301–309. https://doi.org/10.1021/am302097b

[50] Bapna K, Phase DM, Choudhary RJ (2011) Study of valence band structure of Fe doped anatase TiO_2 thin films. J Appl Phys 110:043910. https://doi.org/10.1063/1.3624775

[51] Feng N, Liu F, Huang M et al (2016) Unravelling the efficient photocatalytic activity of boron-induced Ti^{3+}species in the surface layer of TiO_2. Sci Rep 6:34765. https://doi.org/10.1038/srep34765

[52] Weidler N, Schuch J, Knaus F et al (2017) X-ray photoelectron spectroscopic investigation of plasma-enhanced chemical vapor deposited NiO_x, $NiO_x(OH)_y$, and $CoNiO_x(OH)_y$: influence of the chemical composition on the catalytic activity for the oxygen evolution reaction. J Phys Chem C 121:6455–6463. https://doi.org/10.1021/acs.jpcc.6b12652

[53] Vásquez GC, Maestre D, Cremades A et al (2018) Understanding the effects of Cr doping in rutile TiO_2 by DFT calculations and X-ray spectroscopy. Sci Rep 8:1–12. https://doi.org/10.1038/s41598-018-26728-3

[54] Selli D, Fazio G, Di Valentin C (2017) Using density functional theory to model realistic TiO_2 nanoparticles, their photoactivation and interaction with water. Catal 7:357. https://doi.org/10.3390/CATAL7120357

[55] Zhang YH, Reller A (2002) Phase transformation and grain growth of doped nanosized titania. Mater Sci Eng C 19:323–326. https://doi.org/10.1016/S0928-4931(01)00409-X

[56] Nair J, Nair P, Mizukami F et al (1999) Microstructure and phase transformation behavior of doped nanostructured titania. Mater Res Bull 34:1275–1290. https://doi.org/10.1016/S0025-5408(99)00113-0

[57] Spurr RA, Myers H (1957) Quantitative analysis of anatase-rutile mixtures with an X-ray diffractometer. Anal Chem 29:760–762

[58] Kim JY, Jung HS, No JH et al (2006) Influence of anatase-rutile phase transformation on dielectric properties of sol-gel derived TiO_2 thin films. Journal of electroceramics. Springer, Berlin, pp 447–451